

## Article

# Physical, Chemical and Geotechnical Characterization of Wet Flue Gas Desulfurization Gypsum and Its Potential Application as Building Materials

Thandiwe Sithole <sup>1,\*</sup>, Tebogo Mashifana <sup>1</sup> , Dumisane Mahlangu <sup>1</sup>  and Leonel Tchadjie <sup>2</sup>

<sup>1</sup> Department of Chemical Engineering, The University of Johannesburg, P.O. Box 17011, Doornfontein 2088, South Africa; tmashifana@uj.ac.za (T.M.); emmanueldumisane@gmail.com (D.M.)

<sup>2</sup> Department of Civil Engineering Science, The University of Johannesburg, P.O. Box 524, Auckland Park, Johannesburg 2088, South Africa; leonelt@uj.ac.za

\* Correspondence: nastassias@uj.ac.za

**Abstract:** In South Africa, coal represents the primary source of energy used for electricity generation. Coal power plants use the wet flue gas desulfurization (WFGD) process to remove sulfur dioxide (SO<sub>2</sub>) from their flue gas. However, this technology produces a large amount of synthetic gypsum, resulting in waste disposal and environmental pollution. This study investigated the physical, chemical and geotechnical properties of WFGD gypsum and its potential application to develop cement-free bricks. WFGD gypsum was collected from a coal power plant in South Africa. It was found that the principal oxides of WFGD gypsum were sulfur trioxide (SO<sub>3</sub>) and calcium oxide (CaO), which represented more than 90% of the total weight. Calcium sulfate (CaSO<sub>4</sub>) and calcium di aluminate (CA2) were the predominant minerals in the raw material. The density of the WFGD gypsum was 2.43 g/cm<sup>3</sup>. The maximum dry density and optimum moisture content values were 1425 kg/m<sup>3</sup> and 18.5%, respectively. WFGD gypsum had a liquid limit of 51% but did not display any plasticity characteristics. The optimum curing temperature of gypsum bricks was 40 °C. WFGD gypsum-based bricks exhibited compressive strength of up to 2.3 MPa and a density of about 28% less than that of typical clay bricks. Additionally, there was no significant decrease in compressive strength after seven wet/dry cycles. These results show that WFGD gypsum could be used to produce lightweight building materials with low strength requirements.

**Keywords:** gypsum waste; characterization; beneficiation; curing temperature; compressive strength; bricks; microstructure; wet/dry cycles; leaching



**Citation:** Sithole, T.; Mashifana, T.; Mahlangu, D.; Tchadjie, L. Physical, Chemical and Geotechnical Characterization of Wet Flue Gas Desulfurization Gypsum and Its Potential Application as Building Materials. *Buildings* **2021**, *11*, 500. <https://doi.org/10.3390/buildings11110500>

Academic Editor: Łukasz Sadowski

Received: 15 September 2021

Accepted: 13 October 2021

Published: 22 October 2021

**Publisher's Note:** MDPI stays neutral with regard to jurisdictional claims in published maps and institutional affiliations.



**Copyright:** © 2021 by the authors. Licensee MDPI, Basel, Switzerland. This article is an open access article distributed under the terms and conditions of the Creative Commons Attribution (CC BY) license (<https://creativecommons.org/licenses/by/4.0/>).

## 1. Introduction

Human population growth and industrialization have led to a need to generate more electric power [1]. Electricity plants commonly use coal as an inexpensive energy source, but its combustion also causes air pollution. South Africa has the world's highest coal dependency for electricity generation [2–4]. Global warming has become one of the most pressing issues in the 21st century, and it has been significantly influenced by greenhouse gas concentration in the air. South Africa is ranked the second largest sulfur dioxide (SO<sub>2</sub>)-emitting hotspot globally [3]. The technologies for flue gas cleaning systems have undergone developments to reduce atmospheric emissions of hazardous substances. An example of a technology developed is wet flue gas desulfurization (WFGD) [5]. The process involves the removal of SO<sub>2</sub> from flue gas using an alkaline sorbent, usually limestone. Due to its high desulfurization efficiency and low operating costs, the wet limestone system is the most commonly used [6]. However, this technique produces a large quantity of synthetic gypsum, resulting in a problem with waste disposal and pollution. The availability and production of synthetic gypsum will continue as long as thermal power plants exist and use the WFGD process [7]. WFGD gypsum is produced in more

than 225 million tons every year on a global scale. In 2008, US and European factories produced almost 30 million tons of WFGD gypsum, of which less than 75% was recycled [8]. This problem necessitates plans to beneficiate, reuse and recycle these waste materials.

WFGD gypsum is mainly composed of sulfate dihydrate ( $\text{CaSO}_4 \cdot 2\text{H}_2\text{O}$ ) [6,9]. Synthetic gypsum and natural gypsum have very similar chemical compositions and can be used for similar purposes. There are many applications for gypsum as construction material. Gypsum is the main ingredient in the production of plaster, blackboard chalk and drywall [6,10]. Gypsum is also used as an admixture to control the setting time of Portland cement (OPC) [10]. Several studies have reported the use of synthetic gypsum for different applications [11]. Leiva et al. [12] showed that WFGD gypsum could be used to manufacture wallboards. Prior to utilizing WFGD gypsum samples, they were calcined for 30 h at 140 °C to produce gypsum in its hemihydrate form ( $\text{CaSO}_4 \cdot 1/2\text{H}_2\text{O}$ ). A paste was prepared with a different water/gypsum mass ratio in the range of 0.5–0.55. It was reported that WFGD gypsum-based panels satisfied the EN 13279-1 minimum compressive strength requirement of 2 MPa and had a higher thermal insulation capacity than commercial gypsum panels. The proportion of  $\text{CaSO}_4 \cdot 1/2\text{H}_2\text{O}$  was shown to be responsible for the obtained mechanical properties. Similarly, Zhao et al. [13] demonstrated that water-resistant blocks made using WFGD gypsum could be obtained. In this study, a combination of sodium silicate, clinker and sodium sulfate was used as an activator. WFGD gypsum was initially calcined to form b-semiwater gypsum. The results showed that the water resistance of gypsum products was significantly enhanced by the addition of slag, fly ash and a liquid activator. They concluded that the optimal properties were obtained by using a 0.56 wt % waterproof modifier and a curing temperature of 60 °C for 16 h, as determined by the orthogonal test. In the composite material, the main hydration products were ettringite and calcium silicate hydrate (CSH). However, without the incorporation of a modifier, hydration resulted in the formation of  $\text{CaSO}_4 \cdot 2\text{H}_2\text{O}$ , resulting in the block's low anti-water resistance. Additionally, Guan et al. [14] investigated the effects of partial replacement of natural gypsum by WFGD gypsum in calcium aluminate cement (CAC). Results indicated that incorporation of WFGD gypsum shortened the setting and was beneficial for early strength development. Two main hydration mechanisms, ettringite production and CAC hydration, influence the hydration process in pastes comprising 5–15 wt % WFGD gypsum. Ettringite formation regulated the hydration process in mixtures containing more than 20 wt % WFGD gypsum. Koper et al. [15] studied the “effect of calcined synthetic gypsum on the setting time and particle size distribution of modified building materials. It was found that the waste synthetic gypsum met the standard conditions related to its setting time. Therefore, it may be a very good construction substitute for natural gypsum, and consequently, it may contribute to environmental protection and the saving and respecting of energy”. Recently, Phutthimethakul et al. [15] demonstrated that adding a small proportion of synthetic gypsum increased the compressive strength of concrete bricks. For example, the addition of 5.5 wt % gypsum gave 28-day compressive strength of up to 45.18 MPa. Construction and demolition trash, as well as oil palm trunks, were employed as coarse and fine aggregates, respectively, in this investigation.

The chemical composition of WFGD gypsum is mainly related to the proportion of limestone used for the desulfurization process and the type of coal used in the boiler [5]. The latter characteristic has a significant effect on the reactivity of WFGD gypsum. [5,11,13]. The WFGD process is a new technology in South Africa, and due to the country's reliance on coal-fired electricity, WFGD gypsum production has increased significantly over the recent year. The majority of this waste is disposed of in landfills, contributing to environmental degradation. To the best of our knowledge, no studies have been conducted on beneficiating WFGD gypsum produced locally. However, recycling WFGD gypsum to develop value-added products could be beneficial to the country both economically and environmentally. This work aimed to study the physical, chemical and geotechnical properties of local WFGD gypsum and its potential application as a sole precursor to develop cement-free bricks.

## 2. Materials and Methods

### 2.1. The Raw Material

WFGD gypsum was collected from a coal power plant in South Africa. The material was oven-dried, then pulverized and homogeneously mixed using an Eriez Magnetic Rotary Riffler.

### 2.2. pH and Density

A 30 g amount of the material was mixed with 100 mL of deionized water and stirred continuously for 15 min, and then the pH was measured. The relative density of WFGD gypsum was measured using a gas pycnometer

### 2.3. Geotechnical Properties

#### 2.3.1. Sieve Analysis

A 700 g amount dry gypsum sample was used for sieve analysis. The sample was pulverized to break the material into individual particles. Samples were washed using a 2 mm sieve, and the remaining sample was determined. A stack of sieves with sizes 4.75, 2.00, 1.18, 0.60, 0.425, 0.300, 0.150 and 0.075 mm was prepared. A bottom pan was placed under the sieve with a mesh size of 0.075 mm. The stack of sieves was shaken using a sieve shaker for 10 min, and the material retained on each sieve was weighed.

#### 2.3.2. Gradation

A 500 g amount of dry sample was sieved with a stack of sieves with apertures (mm) 4.75, 2.36, 0.76, 0.45, 0.3, 0.15 and 0.075. The sample was poured into the stack of sieves from the top. The stack of sieves was shaken using a sieve shaker for 15 min, and material retained on each sieve was weighed. The gypsum retained on the 0.075 mm sieve was washed and oven-dried. ASTM 152-H hydrometer procedure was followed to determine the particle size distribution of finer particles. A 50 g amount of material smaller than 0.075 mm was used for testing. A 4% solution of sodium hexametaphosphate deflocculating agent was prepared, and 125 mL of the agent was then mixed with 50 g of gypsum and allowed to soak for 12 h. An 875 mL volume of distilled water and 125 mL of the deflocculating agent were thoroughly mixed in a 1000 mL cylinder. The temperature of the blend was noted. A hydrometer was set inside the solution, and the recording was taken as the zero correction. A spatula was then used to blend the gypsum/deflocculating agent mix with the slurry being filled into another graduated 1000 mL cylinder with the assistance of a plastic squeeze bottle. Purified water was then supplemented to the imprint. A rubber stopper was placed on the top of the cylinder, and the gypsum/water blend was mixed by turning the cylinder upside down several times. The cylinder was then placed in the water bath at constant temperature next to the cylinder with deflocculating agent and time was recorded immediately at time = 0.25 min, 0.5 min, 1 min, 2 min, 4 min, 8 min, 15 min, 30 min, 1 h, 2 h, 4 h, 8 h, 24 h and 48 h. For reading, the hydrometer was inserted into the cylinder for approximately 30 s before the recording was done.

#### 2.3.3. Compaction Test

The maximum dry density (MDD) and optimal moisture content of the raw material were determined using the standard proctor compaction test, as per ASTM D698. A 6 kg amount of oven-dried material was prepared and divided into 3 samples of equal mass. Each sample was mixed with water to obtain a percentage of moisture content. The mixed specimen was then placed into a 1 L mold in 3 layers, with each layer compacted uniformly by the 2.5 kg proctor hammer 25 times. After compaction, the specimen was extruded from the mold and weighed to determine its bulk density.

#### 2.3.4. Evaluation of Plasticity

The liquid limit (LL), plastic limit (PL) and plasticity index (PI) of WFGD gypsum were determined using the Atterberg limits method as per ASTM D4318. Material passing 0.425 mm sieve was used throughout the test.

Linear shrinkage was determined as follows: 100 g of WFGD gypsum was mixed with water to form a creamy paste and used to fill the shrinkage limit dish coated with petroleum jelly, and the mass was determined. The dish was tapped to release any bubbles and filled with about one-third until full. Samples were first evaluated visually before exposure to an elevated temperature. Note that WFGD gypsum did not show any plasticity characteristics.

#### 2.4. Mix Proportions and Preparation of Bricks

Brick specimens were prepared by mixing WFGD gypsum with water. The water content that gave MDD and OMC was used, which corresponded to a water to binder ratio of 0.19. After mixing, the paste was poured into 50 mm cube molds and compacted. The cube specimens were then cured at ambient temperature, and the highest unconfined compressive strength was tested after 7, 14, 28, 54 and 90 days, respectively. To study the effect of the curing temperature on the strength development of gypsum bricks, fresh specimens after casting were also cured at different temperatures of 40, 80 and 100 °C for 96 h. After curing, the specimens were allowed to cool down, and UCS was determined.

To evaluate the durability performance of gypsum bricks, a wet and dry cycles test was performed on selected cube specimens. Wet and dry cycle tests were conducted by soaking the specimen in water for 24 h, followed by drying at 60 °C for 24 h. The procedure was repeated 10 times, with the UCS of the specimen determined at each cycle.

Compressive strength of the cubes was determined using compression testing equipment with a capacity of 2000 kN at a loading rate of 0.25 MPa/s until failure. Three composite specimens were tested for every batch to ensure reproducibility of results.

#### 2.5. Toxicity Characteristic Leaching Procedure (TCLP)

The environmental impact of the bricks obtained was assessed using TCLP. WFGD gypsum was pulverized and leached with an extraction buffer of acetic acid and sodium hydroxide (pH  $4.93 \pm 0.05$ ) at a liquid/solid ratio of 20:1 [16]. A thermostatic shaker was utilized for the extraction, and the cured composites were subjected to 24 h shaking at  $25 \pm 2$  °C. Samples were then filtered and analyzed for the concentration of heavy metals using atomic absorption spectroscopy (AAS).

#### 2.6. Analytical Techniques

The chemical composition of the raw material was determined using a dispersive X-ray (XRF) spectrometer operating with a rhodium X-ray tube. Mineralogical analysis was performed using SHINGAKU diffractometer set at 40 kV voltage and 40 mA current, with monochromated CuK  $\alpha$  radiation of  $\lambda = 1.54056$  Å. A scanning rate of 0.017 degrees per second was used over the  $2\theta$  range of 4–100 deg. The FTIR analysis was performed using the Shimadzu FTIR 8400 spectrometer. Specimens for FTIR analyses were prepared using the potassium bromide (KBr) pellet technique. Microscopy investigation was performed using a scanning electron microscope (SEM)-coupled EDS detector.

### 3. Results and Discussion

#### 3.1. Physicochemical Properties of WFGD Gypsum

##### 3.1.1. pH and Relative Density

The pH and relative density of WFGD gypsum were 7.2 and 2.43 g/cm<sup>3</sup>, respectively. The pH of the WFGD gypsum substantially affects the unconfined compressive strength (UCS) of the resulting bricks. Usually, a pH above 10 is beneficial for strength development [17,18]. The values of pH and the relative density obtained are similar to those reported in the literature [19,20].

### 3.1.2. Chemical and Mineralogical Composition

The chemical composition of WFGD gypsum is reported in Table 1. WFGD gypsum is mainly composed of CaO (50.8 wt %) and SO<sub>3</sub> (42.7 wt %), followed by SiO<sub>2</sub> and MgO oxides, which count only for 2.0 and 1.06 wt %, respectively. The rest of the elements, such as P<sub>2</sub>O<sub>5</sub>, Fe<sub>2</sub>O<sub>3</sub>, F, TiO<sub>2</sub> and MnO, existed in trace ( $\leq 1.0$  wt %). The high amount of CaO within the WFGD gypsum could be beneficial, as it can contribute to the pozzolanic reaction by improving the performance at later ages [21]. Similar content of CaO was recorded on natural gypsum from the findings of [22]. Moreover, the SO<sub>3</sub> content in WFGD gypsum could affect the setting time when incorporating the OPC depending on its dosages as increasing the heat of hydration followed by the improvement of strength, as observed by Jelini et al. [23]. In addition, the presence of fluorine could also influence the setting time, leading to a decrease in UCS [24]. The chemical composition of WFGD gypsum is similar to previous works, suggesting its use as construction material [25–27].

**Table 1.** Elemental composition of WFGD gypsum.

Component	WFGD Gypsum (wt %)
F	0.42
MgO	1.06
Al <sub>2</sub> O <sub>3</sub>	1.1
SiO <sub>2</sub>	2.0
P <sub>2</sub> O <sub>5</sub>	0.02
SO <sub>3</sub>	42.7
Fe <sub>2</sub> O <sub>3</sub>	0.64
CaO	50.8
TiO <sub>2</sub>	0.1
MnO	0.6

Figure 1 displays the mineral phases contained in WFGD gypsum. The main crystalline phase of WFGD gypsum was gypsum (G), followed by the calcium di aluminate (CD) mineral. Also, some reflection peaks of coesite (C) and yttrium (Y) oxide were recorded as minor mineral phases. The present result (XRD) demonstrated that the prominent reflection peak in the WFGD gypsum corresponds to calcium sulfate (CaSO<sub>4</sub>), with a content of 90%. This agrees with the XRF results reported in Table 1, which also showed CaO and SO<sub>3</sub> as the predominant constituents in WFGD gypsum. A similar observation was reported by Green (2000). Furthermore, Wu et al. [28] detailed in their findings that the presence of calcium di aluminate accelerates the setting time of the material and improves its resistance to chemical attack. Among the impurities detected in WFGD gypsum was coesite (SiO<sub>2</sub>), a mineral generally used in the industrial production of glass and other construction constituents [29].

The infrared spectrum describing the chemical bonding within the WFGD gypsum is depicted in Figure 2. The pronounced absorption band exhibiting high intensity centered at 1108 cm<sup>-1</sup> and 664 cm<sup>-1</sup> corresponds to the typical vibration modes of gypsum hydrate [30,31]. The formation of these bands belonging to gypsum mineral correlates with the results of the XRD analysis. The broad absorption bands at 3398–3502 cm<sup>-1</sup> and 1614–1686 cm<sup>-1</sup> correspond to H-O stretching and bending H-O-H of water molecules, respectively [31,32]. The absorption band located at 876 cm<sup>-1</sup> is attributed to the vibration of the CO<sub>3</sub><sup>2-</sup> group [33]. Additional detected absorption bands at 2359 and 2344 cm<sup>-1</sup> are attributed to the stretching of CH<sub>3</sub> or CH<sub>2</sub> groups [31].

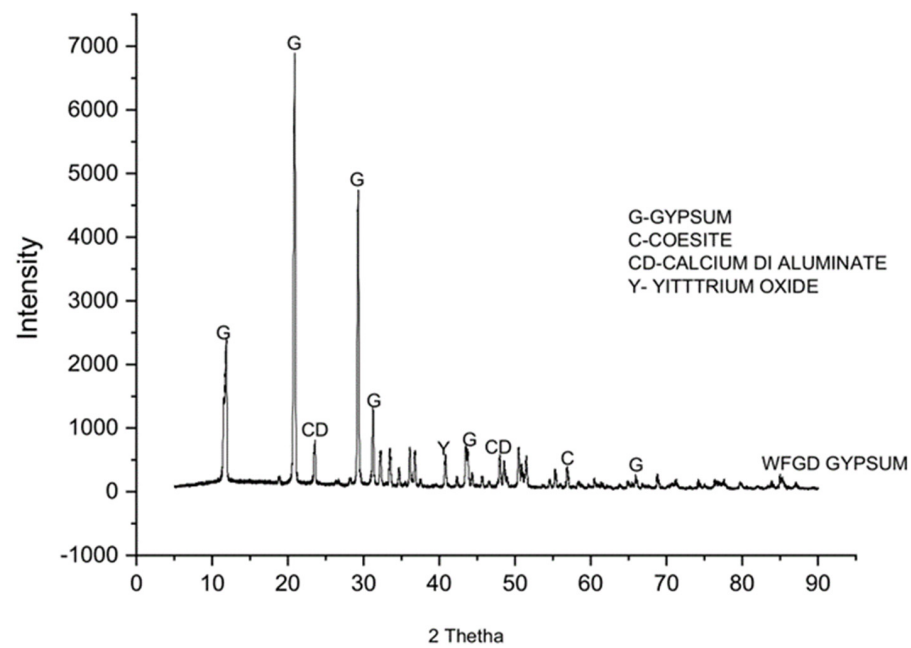


Figure 1. X-ray pattern of WFGD gypsum.

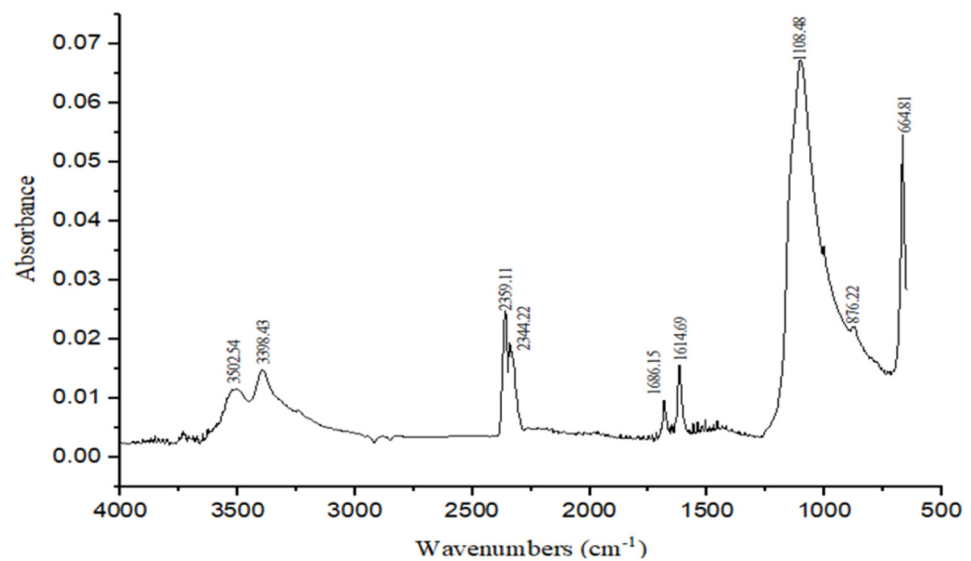
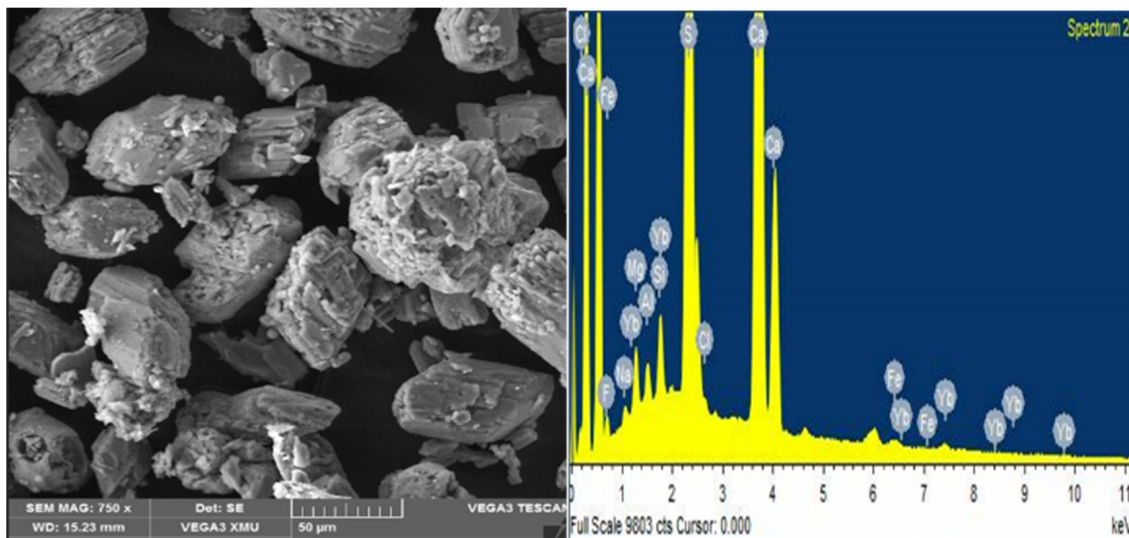


Figure 2. FTIR spectrum of WFGD gypsum.

The SEM and EDS results of raw WFGD gypsum are shown in Figure 3. The microstructure is mainly composed of coarse particles turbulently dispersed in the matrix. The occurrence of twinning structure, asymmetrical particle shapes, rounded fragments and their agglomerates are typical to gypsum crystals detected in the study done by Sharpe and Cork [34]. It is also noticed many lamellar crystals, a couple of quantities of thin prismatic. As indicated by Wahed et al. [35], a large tabular and pseudo-hexagonal molecule is gypsum. The infrequent molded chips on the raw WFGD gypsum represent unburnt carbon typically observed as flat, lamellar, transitional and granular particles, validating that the WFGD gypsum used in the present study has similar characteristics with other WFGD gypsums in the literature [36]. It is illustrated from the EDS spectra that the major elements such as calcium and silica are available, suggesting cementitious properties of the gypsum material [28]. A similar observation has been reported by Wu et al. in their finding based on industrial byproduct gypsum, which showed the presence of calcium and silica as major available elements detected from EDS analysis.



**Figure 3.** SEM and EDS analysis of raw WFGD gypsum.

### 3.1.3. Toxicity Characteristic Leaching Procedure (TCLP)

The leachability of the metals was assessed to determine the viability of using WFGD gypsum. The leaching results of WFGD gypsum (Table 2) showed that the concentration of heavy metals released such as Mn, Cu, Mg, Fe, Al and Cr was negligible and within the limits specified. These results agree with those reported in the literature, indicating that the use of WFGD gypsum for different applications would not contaminate the environment [37,38].

**Table 2.** Leachability of metals from the WFGD gypsum.

Element (%m/m)	WFGD Gypsum
Mn	0.47
Cu	1.56
Mg	1.50
Cr	0.01
Al	0.08
P	0.19
Fe	2.8

## 3.2. Geotechnical Characterization of WFGD Gypsum

### 3.2.1. Particle Size Distribution

Figure 4 illustrates the gradation curve of WFGD gypsum. The average particle diameters  $D_{10}$ ,  $D_{30}$  and  $D_{60}$  were 0.075, 0.10 and 0.15 mm, respectively. Thus, WFGD gypsum mainly consisted of finer particles, as reported in the literature [39]. The uniformity coefficient (Cu) and the coefficient of curvature (Cc) of WFGD gypsum were 2.2 and 1.3, respectively. These coefficients were calculated using Equations (1) and (2). For soil to be considered well graded, the value of Cu should be greater than 4, and Cc should lie between 1 and 3. Accordingly, WFGD gypsum was classified as poorly graded.

$$Cu = \frac{D_{60}}{D_{10}} \quad (1)$$

$$Cc = \frac{1}{D_{10} \times D_{60}} \times D_{30}^2 \quad (2)$$

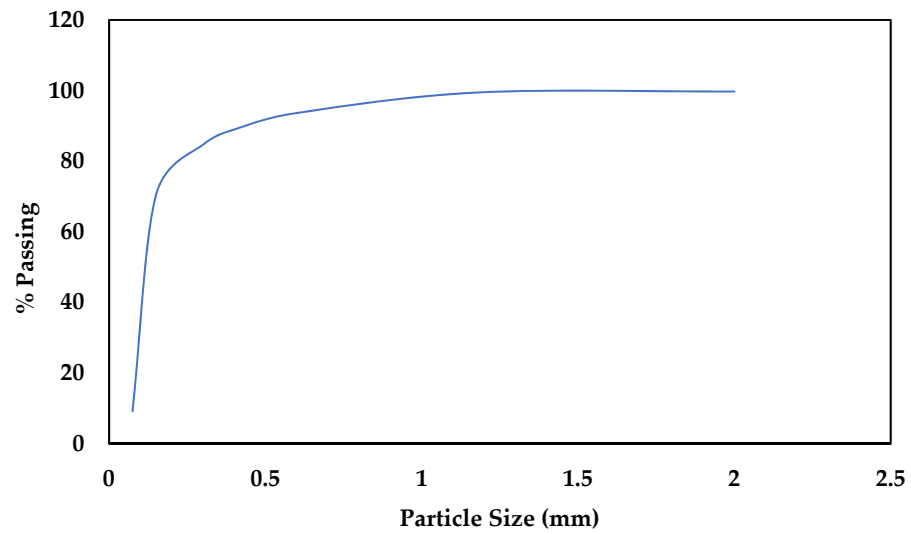


Figure 4. Average gradation of WFGD gypsum.

The volume particle size distribution of WFGD gypsum (Figure 5) is a bimodal volume distribution, with most of the volume of fine particles between 4 and  $100\ \mu\text{m}$ . Note that the finer particles could improve the compressive strength due to the particle packing effect [40,41].

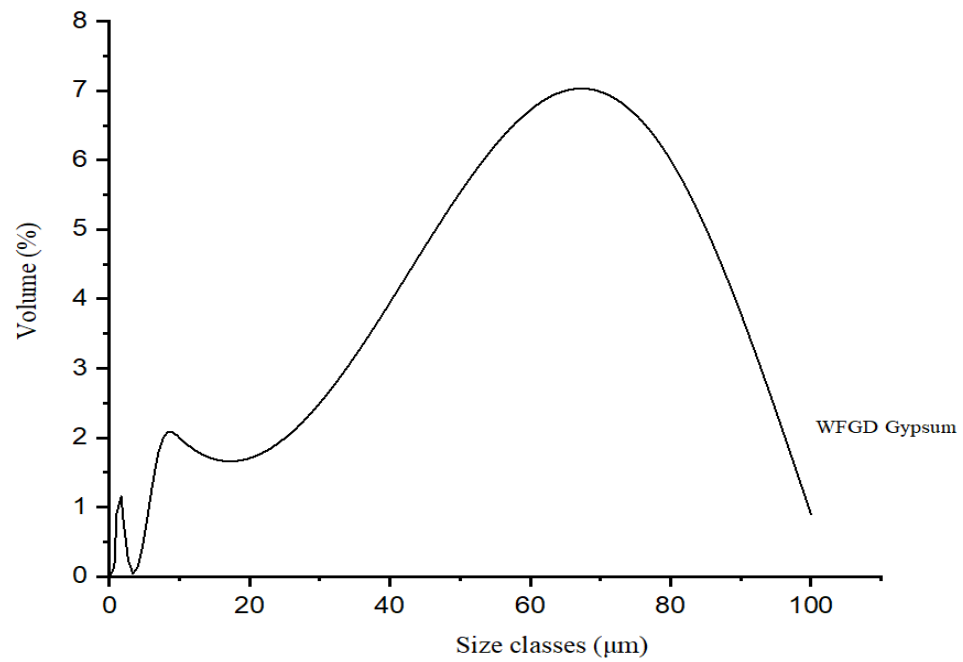


Figure 5. Volume particle size distribution of WFGD gypsum.

### 3.2.2. Maximum Dry Density (MDD) and Optimum Moisture Content (OMC)

Figure 6 gives the compaction curve of WFGD gypsum. The results showed that WFGD gypsum was found to have a maximum dry density (MDD) of  $1425\ \text{kg}/\text{m}^3$  and optimum moisture content (OMC) of 18.5%. The low value of MDD obtained in this study indicates that WFGD gypsum-based bricks are expected to exhibit a low density and poor performance.

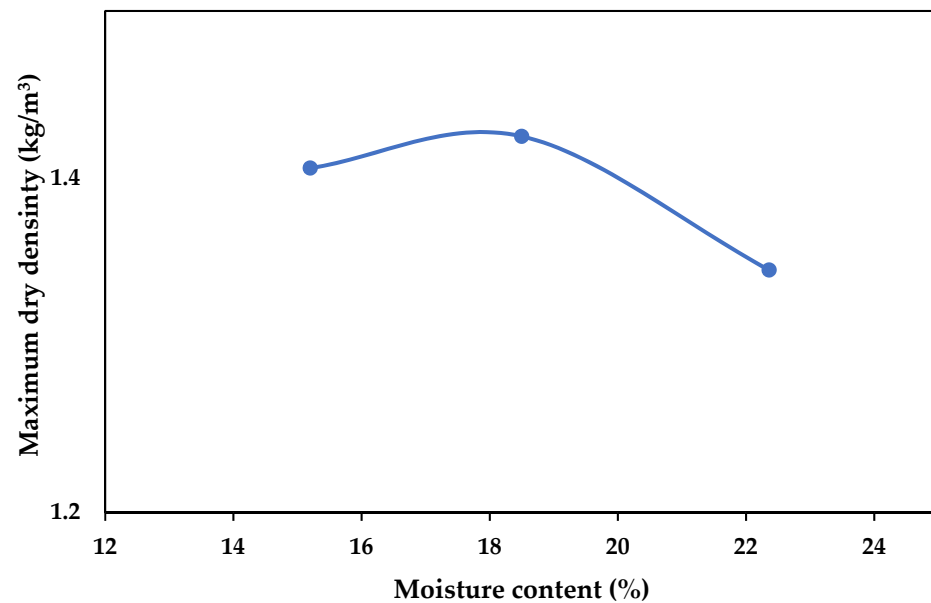


Figure 6. MDD and OMC of WFGD gypsum.

### 3.2.3. Liquid Limit and Plastic Limit Tests

The liquid limit of WFGD gypsum was 51%. WFGD gypsum exhibited nonplastic characteristics. The plastic limit is the moisture content (%) at which a strand of soil will crumble when rolled to a length of 3.18 mm [42]. This lack of plasticity suggests that the clay content was very low [43]. However, despite the low plasticity of WFGD gypsum, it can absorb water just like clay [44]. WFGD gypsum composition varies from plastic to liquid at higher moisture content; consequently, it demands more water for the change to occur [45].

### 3.2.4. Linear Shrinkage

The material was further tested for shrinkage according to ASTM D4943. In this study, shrinkage was assessed through macroscopic contraction of the sample by oven drying the WFGD gypsum mortar and evaluating volume changes. The evolution of the chemical shrinkage indicates faster hydration. WFGD gypsum did not show any signs of shrinkage, indicating that WFGD gypsum specimens have high-volume stability with fewer cracks occurring under drying conditions [46]. This result confirms the nonplastic characteristic exhibited by WFGD gypsum during the plastic limit test. Additionally, the absence of shrinkage suggests the potential of using this waste product as an additive to the improved swelling performance of expansive soils [47].

## 3.3. Characterization of WFGD Gypsum-Based Bricks

### 3.3.1. Effect of Curing Time

#### UCS

Figure 7 shows the effect of long-term curing on the UCS of WFGD gypsum bricks. The long curing did not significantly affect the strength development of the WFGD gypsum material. Increasing the curing age from 7 to 90 days led to an increase in UCS of only 3.1%. This low compressive strength indicates that WFGD gypsum has a very low reactivity at ambient temperature. Nevertheless, the slight strength improvement is related to hydration with C-S-H and ettringite formation in the binder matrix [48,49]. The optimum UCS of the WFGD gypsum is 53% greater than that recorded in the study by Liu et al. [50]. In addition, the developed specimen had a weight of 160 g, which represents a mass 28% smaller than that of a typical clay brick of similar size [51]. Moreover, the highest UCS of 1.99 MPa exhibited by the bricks is above the minimum of 1.5 MPa as specified in SANS 10145

for Class III mortar. Therefore, gypsum bricks could potentially be used as lightweight materials for building and construction applications.

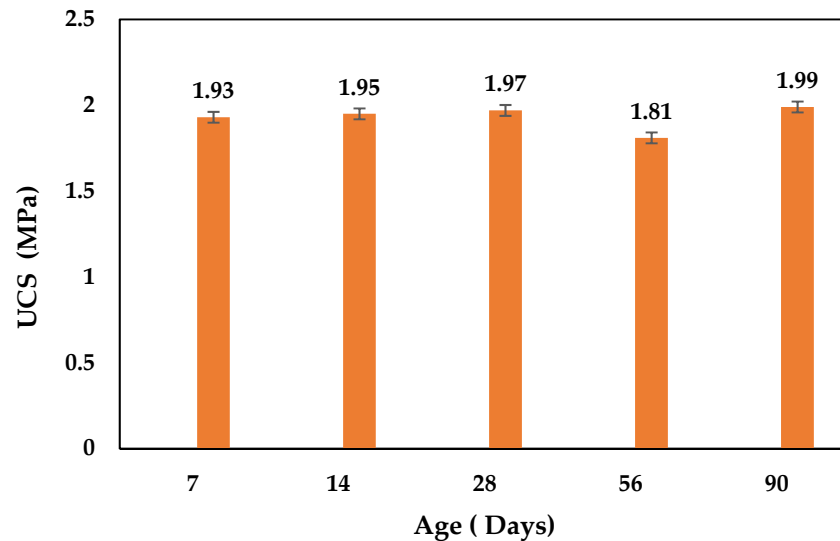


Figure 7. UCS of WFGD gypsum bricks at various curing times.

#### Mineralogy

XRD analysis of WFGD gypsum cured at different ages is presented in Figure 8. The typical mineral phases contained in all six samples are gypsum and quartz. The analysis shows that the main reflection peak in the WFGD gypsum corresponds to calcium sulfate ( $\text{CaSO}_4$ ), with content over 80% in agreement with the existing literature [52–54]. A significant increase in UCS is observed when WFGD gypsum was cured for 90 days. When WFGD gypsum is cured at elevated temperature, there are small reflection peaks of sillimanite formed, and their intensities increase with the temperature rise, resulting in a positive impact on strength development.

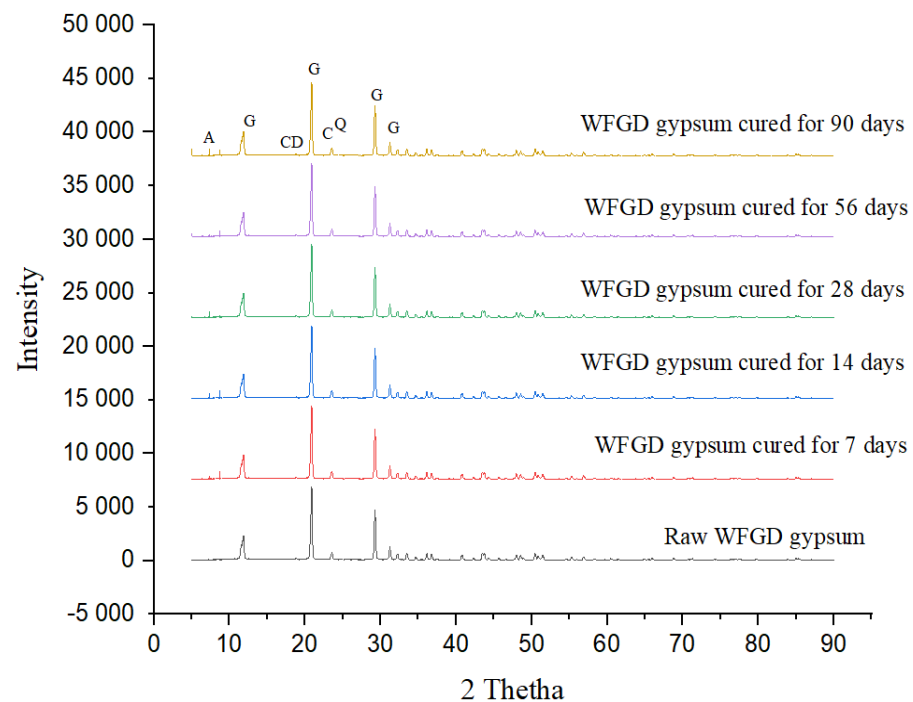
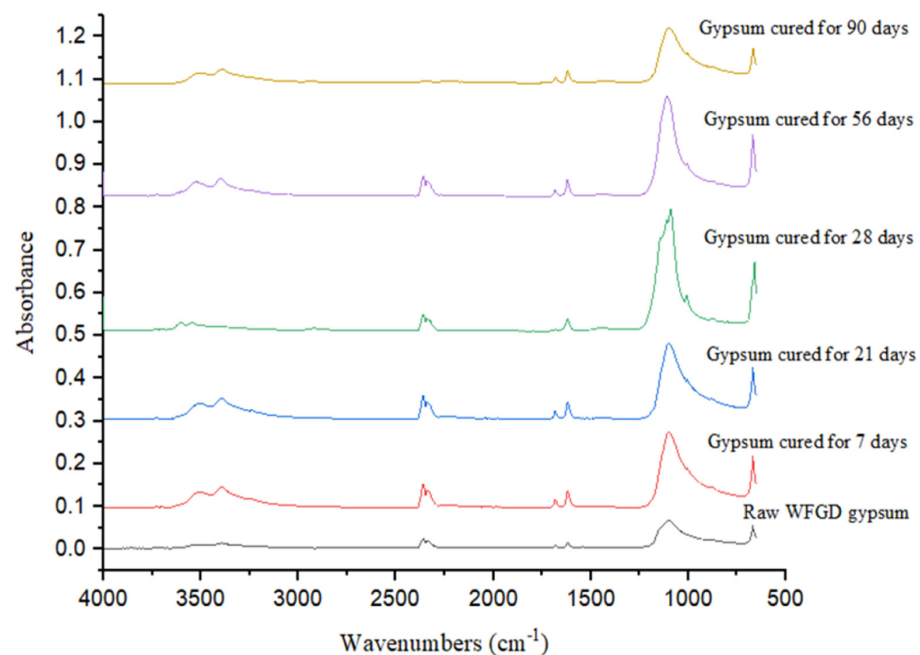


Figure 8. XRD of raw composites cured at ambient temperature (A = sillimanite, Q = quartz, CD = calcium dialuminate, C = coesite).

### FTIR Analysis

Figure 9 displays FTIR spectra of raw WFGD gypsum and WFGD gypsum bricks cured at ambient temperature for different days. The broad absorption band located at  $1223\text{ cm}^{-1}$  is assigned to the C–O stretching mode of the carbonate group ( $\text{CO}_3^{2-}$ ) and a band at  $693\text{ cm}^{-1}$  attributed to the bending mode of gypsum. The sturdy band positioned at  $1240\text{ cm}^{-1}$  and the minor peaks at  $640\text{ cm}^{-1}$  are also allotted to the stretching and bending modes of sulfate, as seen in the pure gypsum spectrum [31]. The bands at  $1200\text{ cm}^{-1}$  and  $873\text{ cm}^{-1}$  are related to the irregular Si–O–Si stretching vibrations and O–Si–O bending vibrations, respectively. There is an occurrence of O=C=O stretching bands, which appear at  $2400\text{ cm}^{-1}$ , except on the WFGD gypsum cured for 90 days. The disappearance of the O=C=O stretching strong bands is a result of insignificant UCS growth [55].



**Figure 9.** FTIR spectra of WFGD gypsum at ambient temperature from 7 to 90 days.

### SEM/EDS Analysis

Figures 10 and 11 show the SEM and EDS analysis of WFGD gypsum cured at different ages for a more extended period. As presented in Figure 10, brick specimens had a heterogeneous microstructure that became more compact with increasing curing time. The specimens cured for 90 days displayed a denser microstructure than other gypsum brick samples. This observation corroborates the highest compressive strength reached following a 90-day curing period. However, after an extended curing time, the shape of raw gypsum particles remained unchanged, indicating a low degree of hydration in the brick specimens [56]. In Figure 11, the intensity belonging to the reflection peaks of C–S–H increased from an early age to later ages. The decrease in the Mn, Fe and K peaks was witnessed when the material was cured for a more extended period under ambient temperature, thus positively enhancing the UCS.

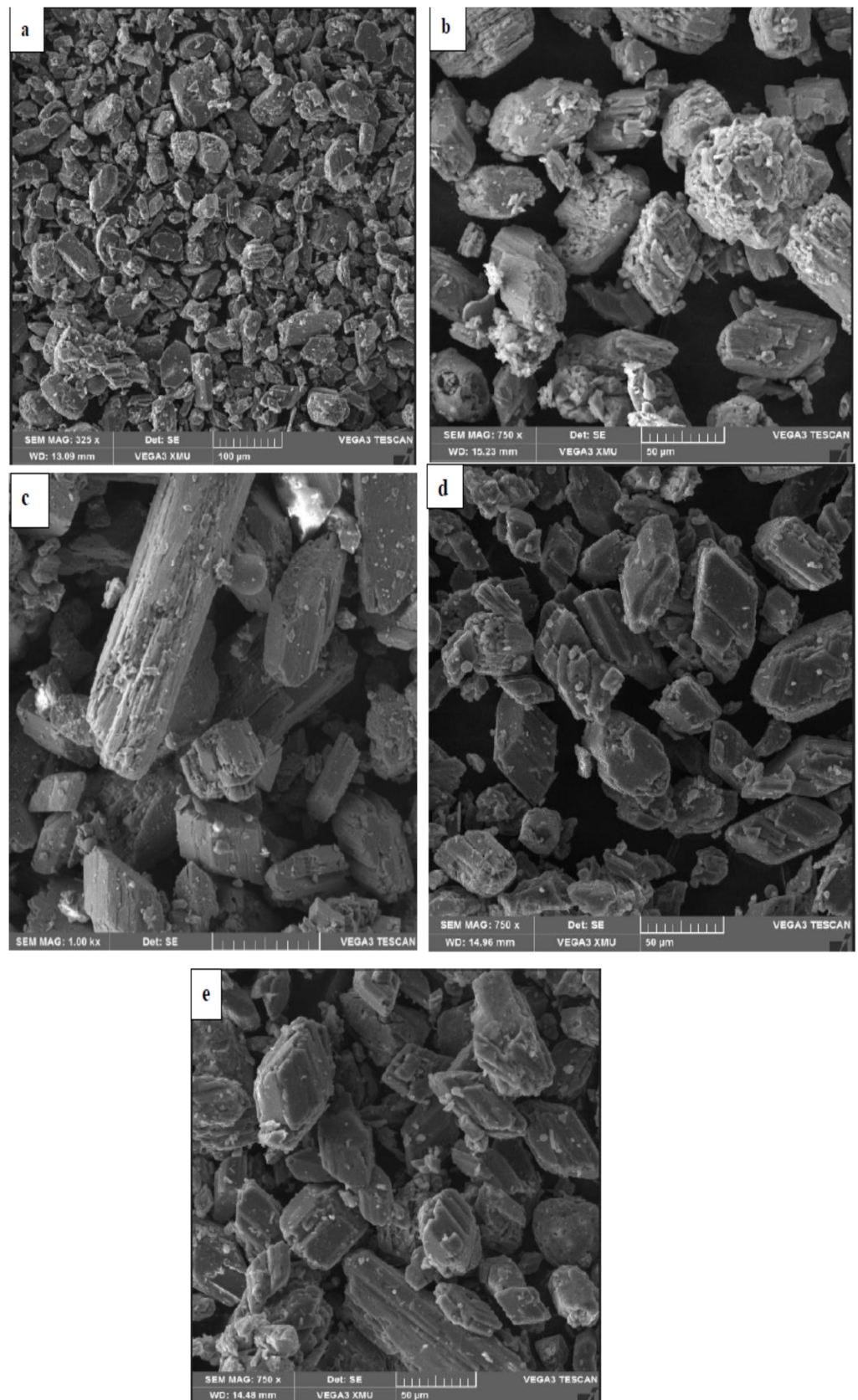


**Figure 10.** SEM analysis of WFGD gypsum cured at ambient temperature ((a) 7 days, (b) 21 days, (c) 28 days, (d) 56 days and (e) 90 days).

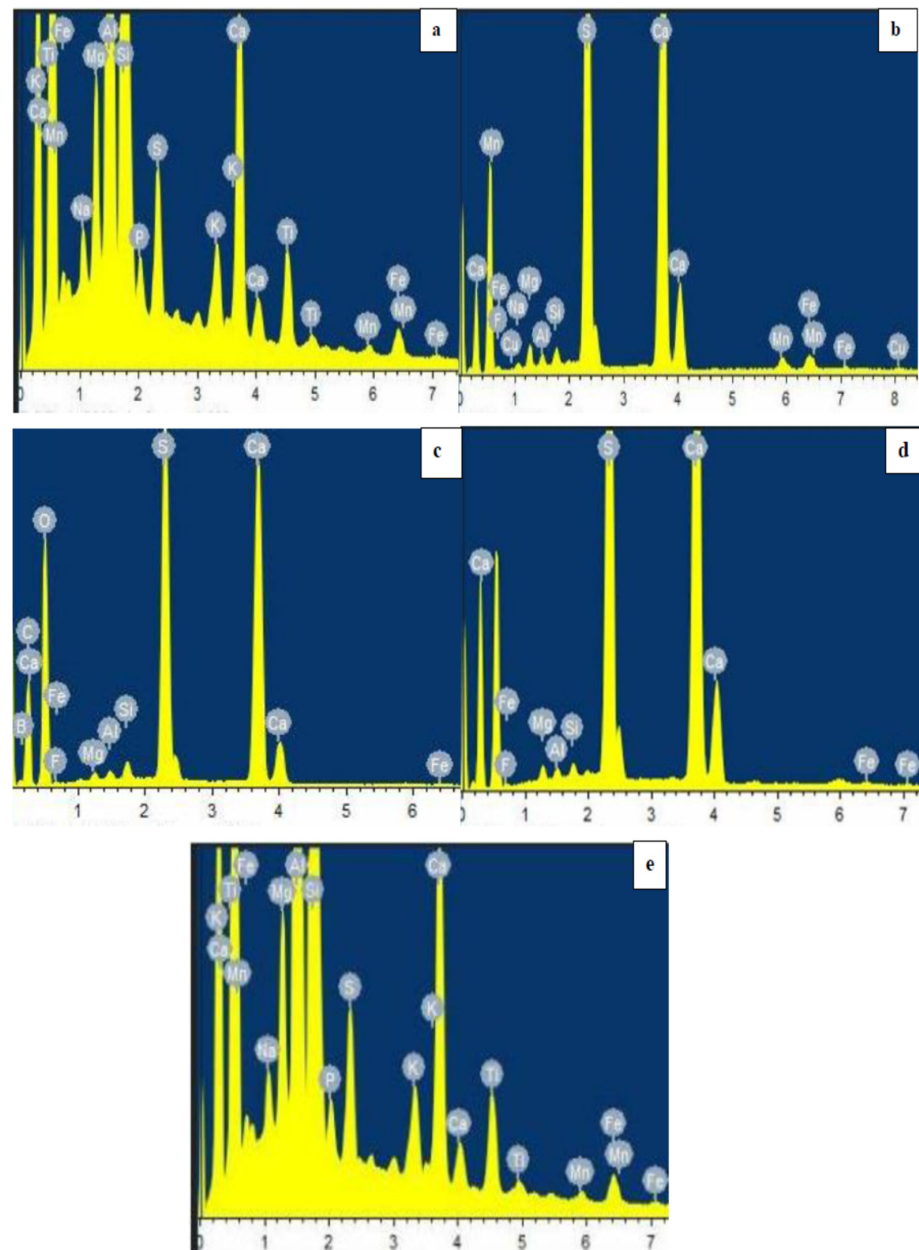


**Figure 11.** EDS analysis of WFGD gypsum cured at ambient temperature ((a) 7 days, (b) 21 days, (c) 28 days, (d) 56 days and (e) 90 days).

### 3.3.2. The Effect of Curing Temperature UCS

Figure 12 displays the results of UCS recorded on WFGD gypsum bricks cured at various temperatures. It can be seen that UCS data varied between 1.64 and 2.3 MPa. Increasing the curing temperature from 40 to 100 °C reduced the UCS by 28.7%. The reduction in strength could be attributed to the formation of voids and cracks resulting from the evaporation of water when the material is cured at high temperatures [57,58]. The trend in strength evolution with curing temperature is consistent with the existing literature that claims that gypsum boards shrink and crack when exposed to high temperatures [59,60]. The highest compressive strength of 2.3 MPa was achieved at the curing temperature of 40 °C. According to Delgado and Guerrero [61], the minimum UCS for the material used in non-load-bearing walls ranges between 1.3 and 2.1 MPa. This shows that WFGD gypsum bricks are suitable to be used as non-load-bearing walls, according to SANS

10400. However, the cracking of gypsum-based materials at high temperatures affects their thermal stability and cannot be overlooked when estimating the heat resistance of WFGD gypsum board assemblies.

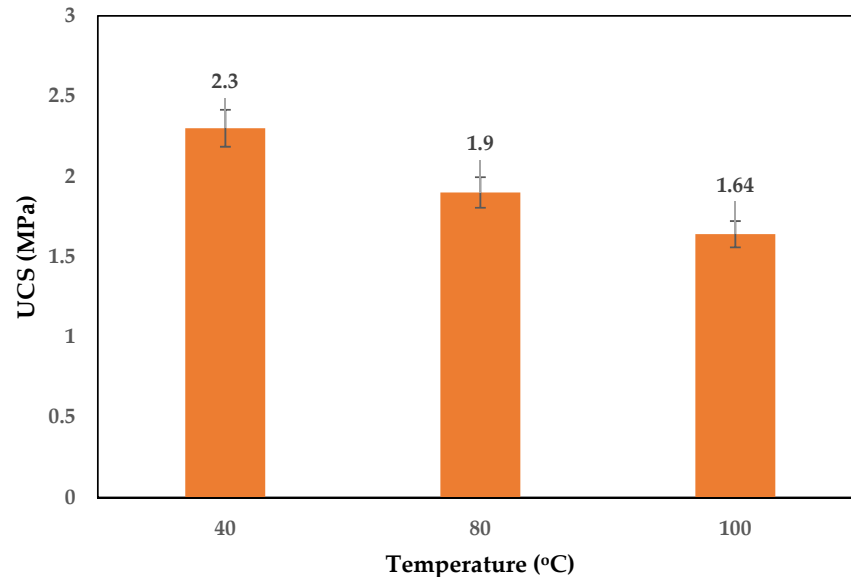


**Figure 12.** UCS of WFGD gypsum bricks at various curing temperatures.

#### Mineralogy

Figure 13 shows XRD analysis of raw WFGD gypsum and WFGD gypsum specimens cured at elevated temperatures (40, 80 and 100 °C). XRD results show that the principal constituents of the binder were gypsum, calcium dialuminate, coesite and sillimanite. The quartz mineral is present due to the fine aggregate particles passing through the sieve when preparing the material. For the sample cured at 40 °C, high reflection peaks of quartz mineral were observed, which contributed to better cohesion with the CSH binding phase, reinforcing the matrix justifying the high strength achieved. This could be the reason why the highest UCS was obtained at 40 °C. A similar result was reported in the study by Hoy et al. [62]. Furthermore, the peak intensity of gypsum decreased when the curing rose from 40 to 100 °C, indicating that this mineral was consumed during the hardening at high temperatures.

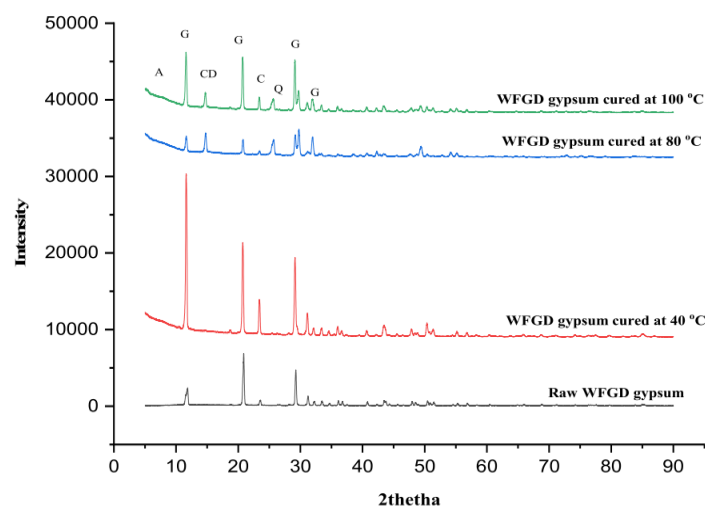


**Figure 13.** X-ray patterns of raw gypsum and those cured at elevated temperatures (A = sillimanite, Q = quartz, CD = calcium dialuminate, C = coesite).

### FTIR Analysis

Figure 14 illustrates the FTIR spectra of WFGD gypsum specimens cured at 40 °C, 80 °C and 100 °C. It is noticed that the differences in intensities of absorption bands observed in Figure 14 with raw WFGD gypsum have less intensity compared to that cured at 100 °C, which exhibits the highest intensity. This behavior could be likely due to the formed  $\gamma$ -CaSO<sub>4</sub> as a result of heating. The main peak at 1100 cm<sup>-1</sup> is assigned to the sulfate in gypsum [30]. The higher the curing temperature, the higher the peak at 1100 cm<sup>-1</sup>, which is due to interactions with major CaSO<sub>4</sub> components. Differences in the shape and altitude of the peaks may be due to hydration or the presence of other atoms other than calcium, especially when heated at higher temperatures [53]. The peak at about 875 cm<sup>-1</sup> for all the graphs corresponds to the vibrational modes of the carbonate group. The far-reaching absorption at 980 cm<sup>-1</sup> is associated with the regular and irregular S–O widening modes (Moutaz, 2005).

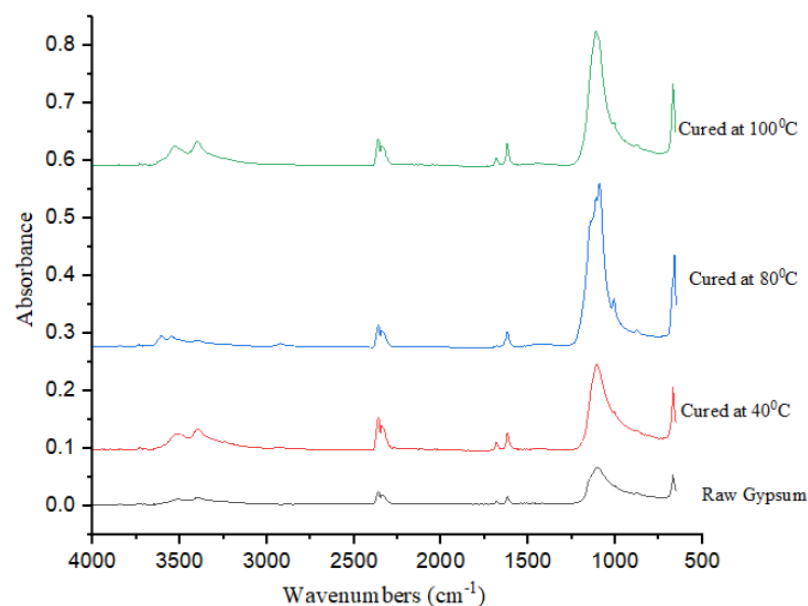
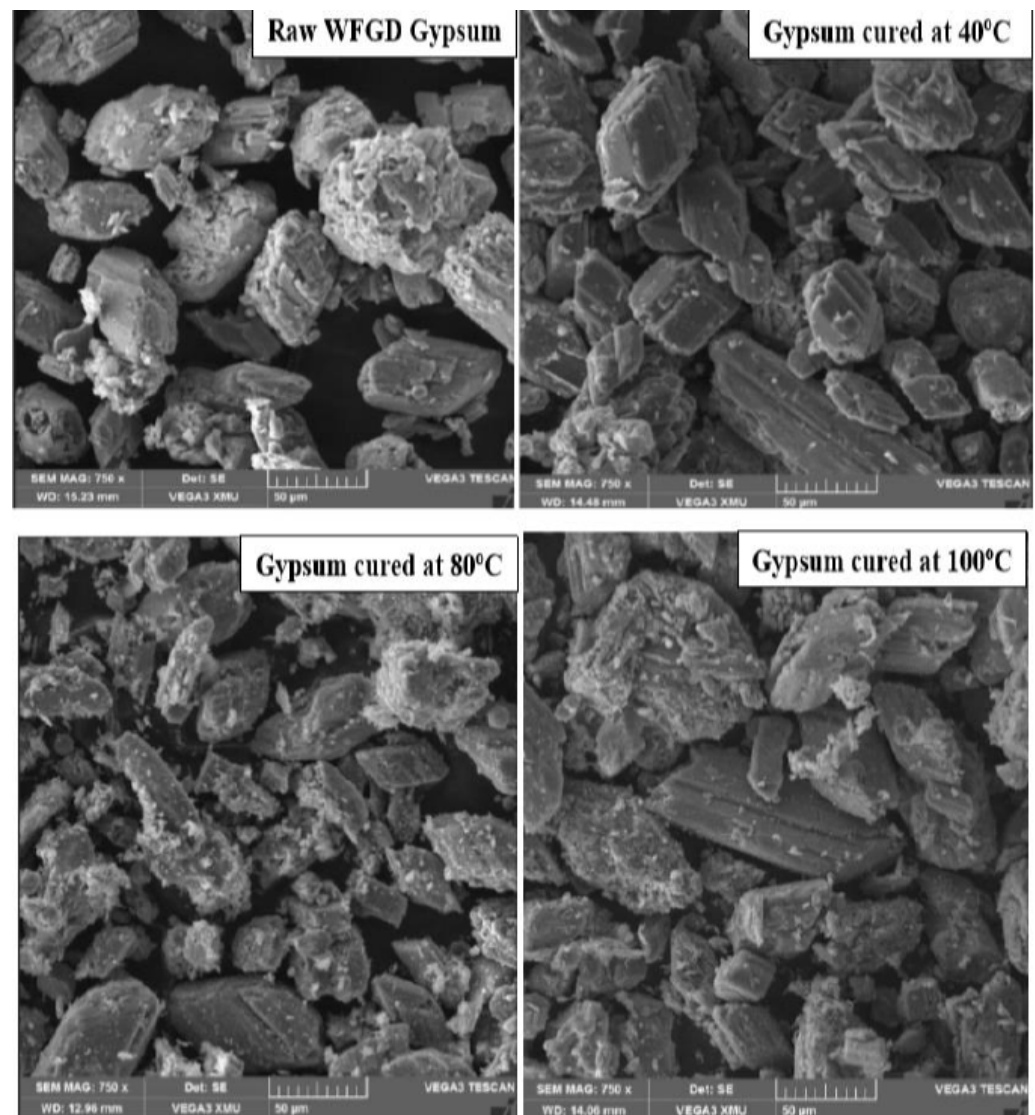


Figure 14. FTIR spectra of WFGD gypsum bricks and elevated temperatures.

### SEM/EDS Analysis

The SEM and EDS analysis of WFGD gypsum cured at elevated temperatures is shown in Figures 15 and 16, respectively. The results validate that gypsum's crystals are not systematic nor homogeneous. As indicated by Wahed et al. [35], large tabular and pseudo-hexagonal molecules signify gypsum. The irregular-shaped chips on the micrograph of raw gypsum Figure 9 represent unburnt carbon from coal typically observed as flat, lamellar, transitional and granular particles [52]. When gypsum was cured at 40 °C, the gypsum particles were turbulently distributed in the matrix. Constituents that enhance the cementation properties of the material, such as calcium and silica, are available in raw WFGD gypsum (Figure 16). Sulfur (S) and phosphorus (P) were also present in the raw gypsum and can impact the strength development. For gypsum bricks cured at 40 °C, strong peaks of Si, Al, Ca and Mg are seen in the EDS spectra. These elements are associated with the formation and stability of CSH, the primary binding phase [63,64]. The peaks of Al, Si and Mg decreased as the curing temperature rose from 40 to 80 °C. This reduction could be attributed to a change in the CSH structure, resulting in poor strength development [65]. Similarly, Gallucci et al. [66] reported that when curing temperatures were increased, the microstructure of the cement paste was significantly coarser and more porous, resulting in lower final strengths.



**Figure 15.** SEM analysis of WFGD gypsum bricks cured at various temperatures.

### 3.3.3. The Durability of WFGD Gypsum Bricks

Figure 17 shows the durability performance of WFGD gypsum specimens cured at ambient temperature for 90 days. The effect of wet and dry cycles on UCS development was investigated. The wet and dry test was carried out for 10 cycles. It can be seen that after the seventh cycle, there was a significant reduction in the UCS due to the specimens' porosity, which resulted in water ingress during soaking. The obtained results show that the developed WFGD gypsum specimens can withstand seven wet and dry cycles and make them potential materials for construction [67]. This result matches quite well with the observations of others, confirming their use in hot and dry climates [68,69].

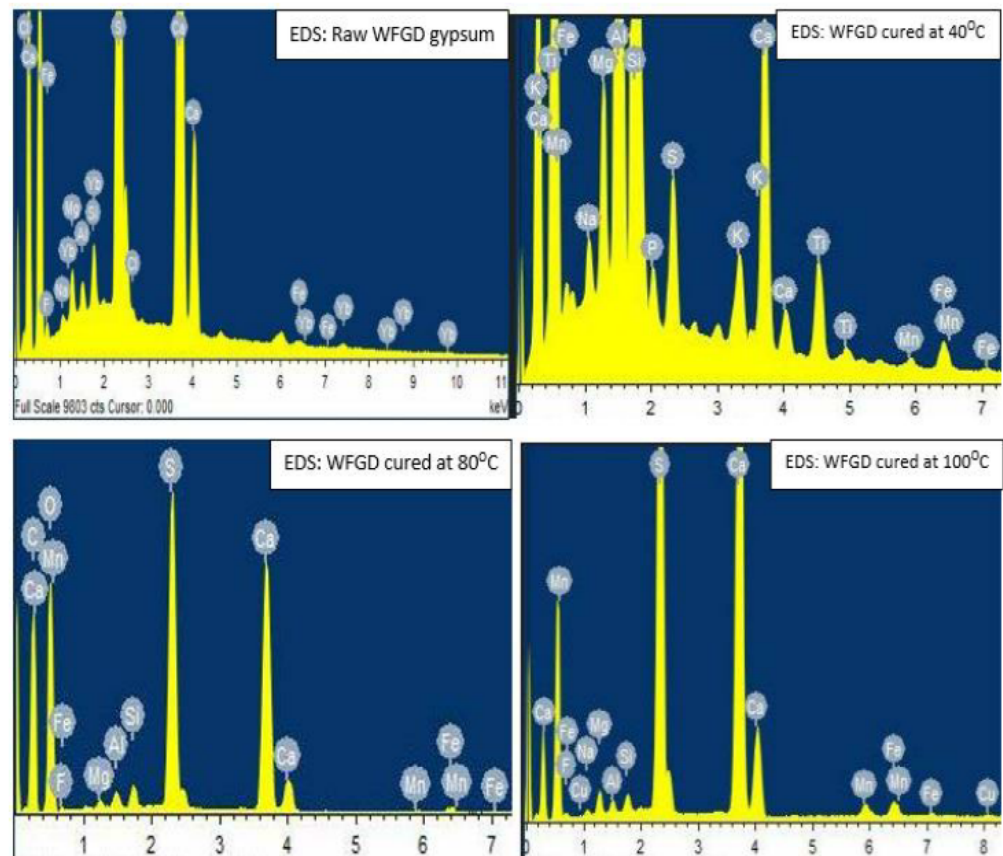


Figure 16. EDS analysis of WFGD gypsum specimens cured at elevated temperatures.

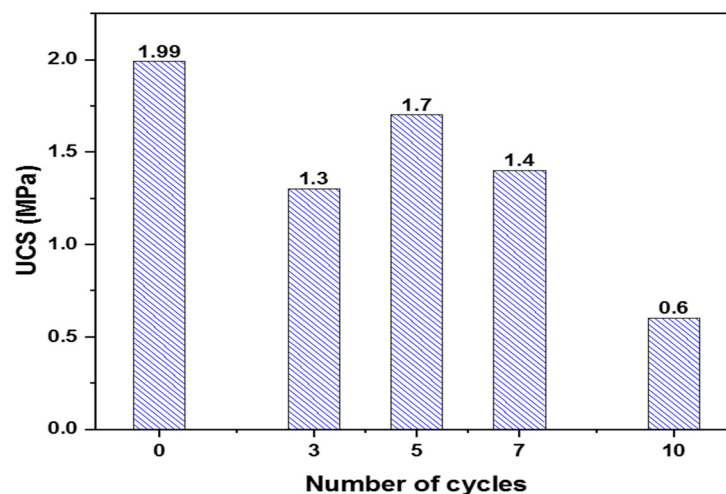


Figure 17. Variation in UCS with wet/dry cycles.

#### 4. Conclusions

In this study, the physical, chemical and geotechnical properties of WFGD gypsum were investigated. The raw material was also used to prepare cement-free bricks. It was found that WFGD gypsum consisted mainly of sulfur and calcium, which had a total weight of more than 90%. The density of WFGD gypsum was  $2.43 \text{ g/cm}^3$ , and its pH was neutral. The material is mainly composed of fine particles, and it was classified as poorly graded. WFGD gypsum had a liquid limit of 51% but did not display any plasticity characteristics. The maximum dry density and optimum moisture content of WFGD gypsum were  $1425 \text{ kg/m}^3$  and 18.5%, respectively. WFGD gypsum-based bricks

exhibited a low strength development at ambient temperature. Higher curing temperatures were detrimental to the strength development of WFGD gypsum because of the formation of cracks within the material. A maximum UCS of 2.3 MPa was obtained at a curing temperature of 40 °C. The durability test showed that WFGD gypsum bricks can withstand seven wet/dry cycles without a significant decrease in compressive strength. The relatively low strength indicates that the brick could be used in non-load-bearing walls as per SANS 10400. Due to the poor reactivity of the WFGD gypsum utilized in this investigation, the following recommendations are suggested. It is worth considering blending WFGD gypsum with other cementitious materials such as fly ash and slag. Additionally, the pretreatment of WFGD gypsum should be examined using thermal or mechanical activation to alter its reactivity.

**Author Contributions:** Supervision, writing—original draft preparation, conceptualization, methodology, validation: T.M.; investigation, data curation, writing—original draft preparation: L.T. and D.M.; co-supervision, conceptualization, writing—review and editing: T.S. All authors have read and agreed to the published version of the manuscript.

**Funding:** This research was funded by the National research foundation (ZA), grant number TTK190312423071/ BAAP200512521382, University Research Committee (URC) and the APC was funded by the University of Johannesburg.

**Data Availability Statement:** Data available within the text of this research paper.

**Acknowledgments:** Many thanks to Metallurgy technical team (Nomsa Baloyi and Joseph Nseke) for their technical support.

**Conflicts of Interest:** The authors declare no conflict of interest. The funders had no role in the design of the study; in the collection, analyses, or interpretation of data; in the writing of the manuscript, or in the decision to publish the results.

## References

1. Schutte, C. Value Added Utilisation Possibilities of Coal Combustion Products in South Africa, North-West University. 2018. Available online: <https://repository.nwu.ac.za/handle/10394/30922> (accessed on 12 October 2021).
2. Haslup, C.J.A. The Velvære: Re-imagining Health & Wellness within Post-Industrial Urban Infrastructure. 2020. Available online: <http://hdl.handle.net/1903/26241> (accessed on 12 October 2021).
3. Conway, D.; Van Garderen, E.A.; Deryng, D.; Dorling, S.; Krueger, T.; Landman, W.; Lankford, B.; Lebek, K.; Osborn, T.; Ringler, C.; et al. Climate and southern Africa's water–energy–food nexus. *Nat. Clim. Chang.* **2015**, *5*, 837–846. [[CrossRef](#)]
4. IEA; WBCSD. *Cement Technology Roadmap 2009: Carbon Emissions Reductions up to 2050*; WBCSD: Paris, France, 2009.
5. Koralegedaraa, N.H.; Pintob, P.X.; Dionysiouc, D.D.; Al-Abed, S.R. Recent advances in flue gas desulfurization gypsum processes and applications—A review. *J. Environ. Manag.* **2019**, *251*, 109572. [[CrossRef](#)]
6. Córdoba, P. Status of Flue Gas Desulphurisation (FGD) systems from coal-fired power plants: Overview of the physic-chemical control processes of wet limestone FGDs. *Fuel* **2015**, *144*, 274–286. [[CrossRef](#)]
7. Jiménez Rivero, A.; Sathre, R.; García Navarro, J. Life cycle energy and material flow implications of gypsum plasterboard recycling in the European Union. *Resour. Conserv. Recycl.* **2016**, *108*, 171–181. [[CrossRef](#)]
8. Malhotra, V.M.J. Role of fly ash in reducing greenhouse gas emissions during the manufacturing of portland cement clinker. *Adv. Concr. Technol. Middle East* **2008**, 19–20.
9. Lei, D.-Y.; Guo, L.-P.; Sun, W.; Liu, J.; Miao, C. Study on properties of untreated FGD gypsum-based high-strength building materials. *Constr. Build. Mater.* **2017**, *153*, 765–773. [[CrossRef](#)]
10. Telesca, A.; Marroccoli, M.; Calabrese, D.; Valenti, G.L.; Montagnaro, F. Flue gas desulfurization gypsum and coal fly ash as basic components of prefabricated building materials. *Waste Manag.* **2013**, *33*, 628–633. [[CrossRef](#)]
11. Álvarez-Ayuso, E.; Querol, X.; Tomás, A. Environmental impact of a coal combustion-desulphurisation plant: Abatement capacity of desulphurisation process and environmental characterisation of combustion by-products. *Chemosphere* **2006**, *65*, 2009–2017. [[CrossRef](#)] [[PubMed](#)]
12. Leiva, C.; García Arenas, C.; Vilches, L.F.; Vale, J.; Gimenez, A.; Ballesteros, J.C.; Fernández-Pereira, C. Use of FGD gypsum in fire resistant panels. *Waste Manag.* **2010**, *30*, 1123–1129. [[CrossRef](#)]
13. Zhao, F.Q.; Liu, H.J.; Hao, L.X.; Li, Q. Water resistant block from desulfurization gypsum. *Constr. Build. Mater.* **2012**, *27*, 531–533. [[CrossRef](#)]
14. Guan, B.; Lou, W.; Ye, Q.; Fu, H.; Wu, Z. Calorimetric study of calcium aluminate cement blended with flue gas desulfurization gypsum. *J. Therm. Anal. Calorim.* **2009**, *98*, 737. [[CrossRef](#)]

15. Phutthimethakul, L.; Kumpueng, P.; Supakata, N. Use of Flue Gas Desulfurization Gypsum, Construction and Demolition Waste, and Oil Palm Waste Trunks to Produce Concrete Bricks. *Crystals* **2020**, *709*, 45–76. [[CrossRef](#)]
16. Anastasiadou, K.; Christopoulos, K.; Mousios, E.; Gidarakos, E. Solidification/stabilization of fly and bottom ash from medical waste incineration facility. *J. Hazard. Mater.* **2012**, *207*, 165–170. [[CrossRef](#)] [[PubMed](#)]
17. Little, D.N. *Evaluation of Structural Properties of lime Stabilized Soils and Aggregates*; National Lime Association: Arlington, VA, USA, 1998.
18. Jafer, H.; Atherton, W.; Sadique, M.; Ruddock, F.; Loffill, E. Stabilisation of soft soil using binary blending of high calcium fly ash and palm oil fuel ash. *Appl. Clay Sci.* **2018**, *152*, 323–332. [[CrossRef](#)]
19. Zhu, F.; Hou, J.; Xue, S.; Wu, C.; Wang, Q.; Hartlew, W. Vermicompost and gypsum amendments improve aggregate formation in bauxite residue. *L. Degrad. Dev.* **2017**, *28*, 2109–2120. [[CrossRef](#)]
20. Raghavendra, S.C.; Raibagkar, R.L.; Kulkarni, A.B. Dielectric properties of fly ash. *Bull. Mater. Sci.* **2002**, *25*, 37–39. [[CrossRef](#)]
21. Scheinherrová, L.; Doleželová, M.; Havlín, J.; Trník, A. Thermal analysis of ternary gypsum-based binders stored in different environments. *J. Therm. Anal. Calorim.* **2018**, *133*, 177–188. [[CrossRef](#)]
22. Madani, H.; Bagheri, A.; Parhizkar, T. The pozzolanic reactivity of monodispersed nanosilica hydrosols and their influence on the hydration characteristics of Portland cement. *Cem. Concr. Res.* **2012**, *42*, 1563–1570. [[CrossRef](#)]
23. Jelenić, I.; Panović, A.; Halle, R.; Gačeša, T. Effect of gypsum on the hydration and strength development of commercial portland cements containing alkali sulfates. *Cem. Concr. Res.* **1977**, *7*, 239–245. [[CrossRef](#)]
24. Al-Bedoor, A.A.; Al-Rawajfeh, A.E.; Jaradat, D.M.M.; Al-Jaradeen, Y.; Al-Obeidein, A. Influence of retardation and acceleration of setting time on the efficiency of water defluoridation by calcined gypsum. *Int. J. Environ. Sci. Technol.* **2017**, *14*, 1551–1558. [[CrossRef](#)]
25. Tzouvalas, G.; Rantis, G.; Tsimas, S. Alternative calcium-sulfate-bearing materials as cement retarders: Part II. FGD gypsum. *Cem. Concr. Res.* **2004**, *34*, 2119–2125. [[CrossRef](#)]
26. Ozkul, M.H. Utilization of citro- and desulphogypsum as set retarders in Portland cement. *Cem. Concr. Res.* **2000**, *30*, 1755–1758. [[CrossRef](#)]
27. Lou, W.; Guan, B.; Wu, Z. Dehydration behavior of FGD gypsum by simultaneous TG and DSC analysis. *J. Therm. Anal. Calorim.* **2011**, *104*, 661–669. [[CrossRef](#)]
28. Wu, S.; Yao, Y.; Yao, X.; Ren, C.; Li, J.; Xu, D.; Wang, W. Co-preparation of calcium sulfoaluminate cement and sulfuric acid through mass utilization of industrial by-product gypsum. *J. Clean. Prod.* **2020**, *265*, 121801. [[CrossRef](#)]
29. Yilmaz, G. Structural characterization of glass–ceramics made from fly ash containing SiO<sub>2</sub>–Al<sub>2</sub>O<sub>3</sub>–Fe<sub>2</sub>O<sub>3</sub>–CaO and analysis by FT-IR–XRD–SEM methods. *J. Mol. Struct.* **2012**, *1019*, 37–42. [[CrossRef](#)]
30. Bishop, J.L.; Lane, M.D.; Dyar, M.D.; King, S.J.; Brown, A.J.; Swayze, G.A. Spectral properties of Ca-sulfates: Gypsum, bassanite, and anhydrite. *Am. Mineral.* **2014**, *99*, 2105–2115. [[CrossRef](#)]
31. La Russa, M.F.; Ruffolo, S.A.; Barone, G.; Crisci, G.M.; Mazzoleni, P.; Pezzino, A. The Use of FTIR and Micro-FTIR Spectroscopy: An Example of Application to Cultural Heritage. *Int. J. Spectrosc.* **2009**, *2009*, 893528. [[CrossRef](#)]
32. Seidl, V.; Knop, O.; Falk, M. Infrared studies of water in crystalline hydrates: Gypsum, CaSO<sub>4</sub>•2H<sub>2</sub>O. *Can. J. Chem.* **1969**, *47*, 1361–1368. [[CrossRef](#)]
33. Gong, K.; White, C.E. Nanoscale chemical degradation mechanisms of sulfate attack in alkali-activated slag. *J. Phys. Chem. C* **2018**, *122*, 5992–6004. [[CrossRef](#)]
34. Sharpe, R.; Cork, G. *Gypsum and Anhydrite; In Industrial Minerals & Rocks*, 7th ed.; Kogel, J., Ed.; Society for Mining, Metallurgy, and Exploration: Englewood, CO, USA, 2006.
35. Abdel Wahed, M.S.M.; Mohamed, E.A.; El-Sayed, M.I.; M’Nif, A.; Sillanpää, M. Crystallization sequence during evaporation of a high concentrated brine involving the system Na–K–Mg–Cl–SO<sub>4</sub>–H<sub>2</sub>O. *Desalination* **2015**, *355*, 11–21. [[CrossRef](#)]
36. Vassilev, S.V.; Vassileva, C.G.; Karayigit, A.I.; Bulut, Y.; Alastuey, A.; Querol, X. Phase–mineral and chemical composition of composite samples from feed coals, bottom ashes and fly ashes at the Soma power station, Turkey. *Int. J. Coal Geol.* **2005**, *61*, 35–63. [[CrossRef](#)]
37. Koralegedara, N.H.; Al-Abed, S.R.; Arambewela, M.K.J.; Dionysiou, D.D. Impact of leaching conditions on constituents release from Flue Gas Desulfurization Gypsum (FGDG) and FGDG–soil mixture. *J. Hazard. Mater.* **2017**, *324*, 83–93. [[CrossRef](#)] [[PubMed](#)]
38. Nugteren, H.W.; Ogundiran, M.B.; Witkamp, G.-J.; Kreutzer, M. Coal fly ash activated by waste sodium aluminate solutions as an immobilizer for hazardous waste. In Proceedings of the 2011 World Coal Ash WOCA Conference, Denver, CO, USA, 9–12 May 2011; pp. 9–11.
39. Fu, B.; Liu, G.; Mian, M.M.; Sun, M.; Wu, D. Characteristics and speciation of heavy metals in fly ash and FGD gypsum from Chinese coal-fired power plants. *Fuel* **2019**, *251*, 593–602. [[CrossRef](#)]
40. Kroehong, W.; Sinsiri, T.; Jaturapitakkul, C.; Chindaprasirt, P. Effect of palm oil fuel ash fineness on the microstructure of blended cement paste. *Constr. Build. Mater.* **2011**, *25*, 4095–4104. [[CrossRef](#)]
41. Ding, X.; Zhang, L. A new contact model to improve the simulated ratio of unconfined compressive strength to tensile strength in bonded particle models. *Int. J. Rock Mech. Min. Sci.* **2014**, *69*, 111–119. [[CrossRef](#)]
42. Hallett, P.D.; Bengough, A.G. Managing the soil physical environment for plants. *Soil Cond.* **2013**, 238–268.

43. Taylor, M.; Kim, N.; Smidt, G.; Busby, C.; McNally, S.; Robinson, B.; Kratz, S.; Schnug, E. Trace element contaminants and radioactivity from phosphate fertiliser. In *Phosphorus in Agriculture: 100% Zero*; Springer: Berlin/Heidelberg, Germany, 2016; pp. 231–266.
44. Coo, J.L.; So, Z.P.S.; Ng, C.W.W. Effect of nanoparticles on the shrinkage properties of clay. *Eng. Geol.* **2016**, *213*, 84–88. [[CrossRef](#)]
45. Sharma, N.K.; Swain, S.K.; Sahoo, U.C. Stabilization of a clayey soil with fly ash and lime: A micro level investigation. *Geotech. Geol. Eng.* **2012**, *30*, 1197–1205. [[CrossRef](#)]
46. Prashanth, J.P.; Sivapullaiah, P.V.; Sridharan, A. Pozzolanic fly ash as a hydraulic barrier in land fills. *Eng. Geol.* **2001**, *60*, 245–252. [[CrossRef](#)]
47. Yilmaz, I.; Civelekoglu, B. Gypsum: An additive for stabilization of swelling clay soils. *Appl. Clay Sci.* **2009**, *44*, 166–172. [[CrossRef](#)]
48. Bullard, J.W.; Jennings, H.M.; Livingston, R.A.; Nonat, A.; Scherer, G.W.; Schweitzer, J.S.; Scrivener, K.L.; Thomas, J.J. Mechanisms of cement hydration. *Cem. Concr. Res.* **2011**, *41*, 1208–1223. [[CrossRef](#)]
49. Maichin, P.; Jitsangiam, P.; Nongnuang, T.; Boonserm, K.; Nusit, K.; Pra-Ai, S.; Binaree, T.; Aryupong, C. Stabilized High Clay Content Lateritic Soil Using Cement-FGD Gypsum Mixtures for Road Subbase Applications. *Materials* **2021**, *14*, 1858. [[CrossRef](#)] [[PubMed](#)]
50. Liu, X.; Wen, H.; Edil, T.; Benson, C.H. Stabilization of flue gas desulfurization by-products with fly ash, cement, and sialite. *Transp. Res. Rec.* **2011**, *2204*, 102–109. [[CrossRef](#)]
51. Mainuddin, M.; Ruhul Amin, M.; Sarkhel, S.; Bhowmick, P.; Ahmed, A. Stresses in Fly Ash Brick using different proportion of Lime, Cement, Gypsum, Sand and Stone Dust. *Int. J. Innov. Technol. Explor. Eng.* **2019**, *9*, 4288–4292. [[CrossRef](#)]
52. Pedreño-Rojas, M.A.; De Brito, J.; Flores-Colen, I.; Pereira, M.F.C.; Rubio-de-Hita, P. Influence of gypsum wastes on the workability of plasters: Heating process and microstructural analysis. *J. Build. Eng.* **2020**, *29*, 101143. [[CrossRef](#)]
53. Harrison, T.N. Experimental VNIR reflectance spectroscopy of gypsum dehydration: Investigating the gypsum to bassanite transition. *Am. Mineral.* **2012**, *97*, 598–609. [[CrossRef](#)]
54. Pedreño-Rojas, M.A.; Fořt, J.; Černý, R.; Rubio-de-Hita, P. Life cycle assessment of natural and recycled gypsum production in the Spanish context. *J. Clean. Prod.* **2020**, *253*, 120056. [[CrossRef](#)]
55. Lv, Q.; Wang, Z.; Gu, L.; Chen, Y.; Shan, X. Effect of sodium sulfate on strength and microstructure of alkali-activated fly ash based geopolymer. *J. Cent. South Univ.* **2020**, *27*, 1691–1702. [[CrossRef](#)]
56. Wang, T.; Wu, K.; Wu, M. Development of green binder systems based on flue gas desulfurization gypsum and fly ash incorporating slag or steel slag powders. *Constr. Build. Mater.* **2020**, *265*, 120275. [[CrossRef](#)]
57. Salvador, R.P. Accelerated Cementitious Matrices: Hydration, Microstructure and Mechanical Strength. 2016. Available online: <http://hdl.handle.net/2117/106491> (accessed on 12 October 2021).
58. Little, T.A.; Holcombe, R.J.; Ilg, B.R. Kinematics of oblique collision and ramping inferred from microstructures and strain in middle crustal rocks, central Southern Alps, New Zealand. *J. Struct. Geol.* **2002**, *24*, 219–239. [[CrossRef](#)]
59. Ridge, M.J. Effect of Temperature on the Rate of Setting of Gypsum Plaster. *Nature* **1959**, *184*, 47–48. [[CrossRef](#)]
60. Thomas, G. Thermal properties of gypsum plasterboard at high temperatures. *Fire Mater.* **2002**, *26*, 37–45. [[CrossRef](#)]
61. Jiménez Delgado, M.C.; Guerrero, I.C. The selection of soils for unstabilised earth building: A normative review. *Constr. Build. Mater.* **2007**, *21*, 237–251. [[CrossRef](#)]
62. Hoy, M.; Rachan, R.; Horpibulsuk, S.; Arulrajah, A.; Mirzababaei, M. Effect of wetting–drying cycles on compressive strength and microstructure of recycled asphalt pavement—Fly ash geopolymer. *Constr. Build. Mater.* **2017**, *144*, 624–634. [[CrossRef](#)]
63. Barzgar, S.; Lothenbach, B.; Mohammed, T.; Ludwig, C. Effect of Aluminum on C-S-H Structure, Stability and Solubility. In Proceedings of the 15th International Congress on the Chemistry of Cement, Prague, Czech Republic, 16–20 September 2019; pp. 1–6.
64. Li, J.; Yu, Q.; Huang, H.; Yin, S. Effects of Ca/Si ratio, aluminum and magnesium on the carbonation behavior of calcium silicate hydrate. *Materials* **2019**, *12*, 1268. [[CrossRef](#)]
65. Pedrosa, H.C.; Reales, O.M.; Reis, V.D.; das Dores Paiva, M.; Fairbairn, E.M.R. Hydration of Portland cement accelerated by C-S-H seeds at different temperatures. *Cem. Concr. Res.* **2020**, *129*, 105978. [[CrossRef](#)]
66. Gallucci, E.; Zhang, X.; Scrivener, K.L. Effect of temperature on the microstructure of calcium silicate hydrate (C-S-H). *Cem. Concr. Res.* **2013**, *53*, 185–195. [[CrossRef](#)]
67. Falayi, T.; Okonta, F.N.; Ntuli, F. The geotechnical and microstructural properties of desilicated fly ash lime stabilised expansive soil. *Mater. Struct.* **2016**, *49*, 4881–4891. [[CrossRef](#)]
68. Djobo, J.N.Y.; Elimbi, A.; Tchakouté, H.K.; Kumar, S. Mechanical properties and durability of volcanic ash based geopolymer mortars. *Constr. Build. Mater.* **2016**, *124*, 606–614. [[CrossRef](#)]
69. Rodrigue Kaze, C.; Ninla Lemougna, P.; Alomayri, T.; Assaedi, H.; Adesina, A.; Kumar Das, S.; Lecomte-Nana, G.L.; Kamseu, E.; Chinje Melo, U.; Leonelli, C. Characterization and performance evaluation of laterite based geopolymer binder cured at different temperatures. *Constr. Build. Mater.* **2021**, *270*, 121443. [[CrossRef](#)]